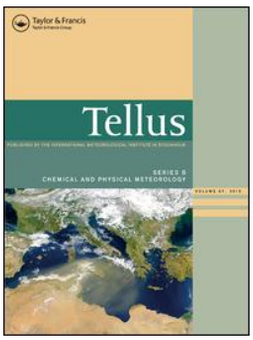

Tellus B: Chemical and Physical Meteorology

ISSN: (Print) (Online) Journal homepage: https://www.tandfonline.com/loi/zelb20

Characterisation of methane sources in Lutjewad, The Netherlands, using quasi-continuous isotopic composition measurements

Malika Menoud , Carina van der Veen , Bert Scheeren , Huilin Chen , Barbara Szénási , Randulph P. Morales , Isabelle Pison , Philippe Bousquet , Dominik Brunner & Thomas Röckmann

To cite this article: Malika Menoud , Carina van der Veen , Bert Scheeren , Huilin Chen , Barbara Szénási , Randulph P. Morales , Isabelle Pison , Philippe Bousquet , Dominik Brunner & Thomas Röckmann (2020) Characterisation of methane sources in Lutjewad, The Netherlands, using quasi-continuous isotopic composition measurements, Tellus B: Chemical and Physical Meteorology, 72:1, 1-20, DOI: 10.1080/16000889.2020.1823733

To link to this article: https://doi.org/10.1080/16000889.2020.1823733

Tellus SERIES B CHEMICAL AND PHYSICAL METEOROLOGY
PUBLISHED BY THE INTERNATIONAL METEOROLOGICAL INSTITUTE IN STOCKHOLM

Characterisation of methane sources in Lutjewad, The Netherlands, using quasi-continuous isotopic composition measurements

By MALIKA MENOUD[1]*, CARINA VAN DER VEEN[1], BERT SCHEEREN[2], HUILIN CHEN[2], BARBARA SZÉNÁSI[3], RANDULPH P. MORALES[4], ISABELLE PISON[3], PHILIPPE BOUSQUET[3], DOMINIK BRUNNER[4], and THOMAS RÖCKMANN[1], [1]*Institute for Marine and Atmospheric Research Utrecht (IMAU), Utrecht University, Utrecht, The Netherlands;* [2]*Centre of Isotope Research, University of Groningen, Groningen, The Netherlands;* [3]*Laboratoire des Sciences du Climat et de l'Environnement, Université de Versailles Saint-Quentin, Paris, France;* [4]*Swiss Federal Laboratories for Materials Science and Technology, Empa, Dübendorf, Switzerland*

(Manuscript Received 20 April 2020; in final form 9 September 2020)

ABSTRACT

Despite the importance of methane for climate change mitigation, uncertainties regarding the temporal and spatial variability of the emissions remain. Measurements of CH_4 isotopic composition are used to partition the relative contributions of different emission sources. We report continuous isotopic measurements during 5 months at the Lutjewad tower (north of the Netherlands). Time-series of $\chi(CH_4)$, $\delta^{13}C\text{-}CH_4$, and $\delta D\text{-}CH_4$ in ambient air were analysed using the Keeling plot method. Resulting source signatures ranged from −67.4 to −52.4‰ vs V-PDB and from −372 to −211‰ vs V-SMOW, for $\delta^{13}C$ and δD respectively, indicating a prevalence of biogenic sources. Analysis of isotope and wind data indicated that (i) emissions from off-shore oil and gas platforms in the North Sea were not detected during this period, (ii) CH_4 from fossil fuel related sources was usually advected from the east, pointing towards the Groningen gas field or regions further east in Germany. The results from two atmospheric transport models, CHIMERE and FLEXPART-COSMO, using the EDGAR v4.3.2 and TNO-MACC III emission inventories, reproduce $\chi(CH_4)$ variations relatively well, but the isotope signatures were over-estimated by the model compared to the observations. Accounting for geographical variations of the $\delta^{13}C$ signatures from fossil fuel emissions improved the model results significantly. The difference between model and measured isotopic signatures was larger when using TNO-MACC III compared to EDGAR v4.3.2 inventory. Uncertainties in the isotope signatures of the sources could explain a significant fraction of the discrepancy, thus a better source characterisation could further strengthen the use of isotopes in constraining emissions.

Keywords: methane, isotope ratio mass spectrometry, source isotopic signatures, emission inventories, in-situ measurements

1. Introduction

Anthropogenic greenhouse gas emissions to the atmosphere are the main driver of the current global climate change. Reducing these emissions is therefore a key goal of climate change mitigation policies. Numerous countries committed to reduce emissions of greenhouse gases as part of the 2015 UN Paris Agreement on Climate Change. This agreement sets an objective to limit future warming to 2 °C (if possible 1.5 °C) compared to pre-industrial temperatures. However, according to Nisbet et al. (2019), the increasing trend in methane concentration in the past years represents a severe threat to reach this goal.

Methane (CH_4) is present at relatively low mole fractions in the troposphere: a global average of 1869 ppb in 2018 is reported by the World Meteorological Organization (WMO, 2019). Yet it is an effective greenhouse gas. The Global Warming Potential (GWP) of CH_4

*Corresponding author. e-mail: m.menoud@uu.nl

Citation: Tellus B: 2020, **72**, 1823733, https://doi.org/10.1080/16000889.2020.1823733

is about 30 kg/kg CO_2 over a 100 year time frame and more than 80 over a 20 year horizon (IPCC, 2013). Furthermore, methane has a relatively short lifetime in the troposphere: 9.1 ± 0.9 years (Saunois et al., 2016). Therefore, focusing on the reduction of methane emissions can effectively contribute to climate change mitigation in the near future.

Methane is emitted from various natural and anthropogenic sources at the Earth's surface. They are usually grouped in three categories: biogenic (e.g. agriculture and farming, waste, biogas production, wetlands and inland water systems), thermogenic (fossil fuel extraction, combustion and consumption, geological sources), and pyrogenic (biomass and biofuel burning). The current understanding of the global methane budget (Saunois et al., 2016) is based on the interpretation of long-term high accuracy atmospheric records (e.g. Dlugokencky et al., 2011), and increasingly satellite retrievals (Monteil et al., 2013; Jacob et al., 2016; Hu et al., 2018; Borsdorff et al., 2019), often used in inverse modelling approaches (Bousquet et al., 2006; Bergamaschi et al., 2009; Rigby et al., 2012; Houweling et al., 2014; Pandey et al., 2017). However, information on the emission rates and locations, and the temporal and spatial variability of the different methane sources still includes large uncertainties both at global (Kirschke et al., 2013; Worden et al., 2017; Pandey et al., 2019; Turner et al., 2019) and regional scales (e.g. Bergamaschi et al., 2018). A better quantification of methane sources is crucial to devise efficient climate change mitigation policies.

The different emission sources can be distinguished using the isotopic composition of CH_4, because its stable isotope content (^{13}C and deuterium) depends on the methane formation process. Measurements of isotopic signatures have been used in many studies to characterise the emissions from individual sites or regions (Levin et al., 1993; Tarasova et al., 2006; Beck et al., 2012; Townsend-Small et al., 2016; Zazzeri et al., 2017). They have also been applied to constrain budget changes in the past (Monteil et al., 2011; Rigby et al., 2012; Schaefer et al., 2016; Worden et al., 2017). Whereas most measurements to date have been performed using analysis in the laboratory on collected samples, field-deployable instruments have only become available recently (Santoni et al., 2012; Eyer et al., 2016; Röckmann et al., 2016).

This article reports high-precision in-situ measurements of methane mole fraction and isotopic composition in ambient air using the isotope ratio mass spectrometry (IRMS) system described in Röckmann et al. (2016). The instrument was deployed for 5 months at Lutjewad, in the North of the Netherlands. The notation $\chi(CH_4)$ refers to methane mole fractions in dry ambient air and is given in nmole/mole or parts per billion, ppb. The isotopic composition is reported in δ notation as:

$$\delta = \frac{R_{sample} - R_{standard}}{R_{standard}}$$

R is the ratio between the heavy and light stable isotopes, here $R = \frac{^{13}C}{^{12}C}$ or $R = \frac{^{2}H \text{ or } D}{^{1}H}$. The standard values are $11180.2 \pm 2.8 \times 10^{-6}$ (Vienna Pee Dee Belemnite, V-PDB) and $155.75 \pm 0.08 \times 10^{-6}$ (Vienna Standard Mean Ocean Water, V-SMOW), respectively for the $\frac{^{13}C}{^{12}C}$ and $\frac{^{2}H}{^{1}H}$ ratios (Werner and Brand, 2001). Both δ^{13}C-CH_4 and δD-CH_4 were continuously measured, together with $\chi(CH_4)$ mole fractions in the air with high-precision IRMS (see below).

Previous measurements made in 2014–2015 at the Cabauw tower in the central Netherlands (Röckmann et al., 2016), showed a prevalence of isotopically depleted sources of methane in the footprint of the station, demonstrating a large contribution from agricultural activities. Landfills and natural gas operations were identified as secondary sources. The Lutjewad coastal site is closer to the on-shore and off-shore North Sea oil and gas installations. One goal was to investigate whether emissions from these anthropogenic sources are more important at Lutjewad compared to the Cabauw site. Off-shore gas extraction facilities emit CH_4 through gas flaring, oil loading, as well as fugitive and operational emissions (Riddick et al., 2019). The detection of methane emissions by these sites was discussed in Yacovitch et al. (2018), based on aircraft measurements along the Dutch coast. They crossed a methane plume during a flight, but could not draw a robust conclusion on its origin. They hypothesised that emissions from offshore platforms may result in a broad elevated baseline $\chi(CH_4)$, combined with sharper signals from other local sources. The isotopic measurements in this study are expected to help assess the influence of different sources on these coastal pollution events. The observations are also interpreted by comparison with two atmospheric dispersion models, based on two emissions inventories. The observations are used to evaluate the model performance and to test our understanding of methane sources and their isotopic signatures in the Netherlands and the surrounding regions.

2. Methodology

2.1. Study site

From the 3rd of November 2016 to the 31st of March 2017, measurements of $\chi(CH_4)$, δ^{13}C-CH_4, and δD-CH_4 in ambient air were conducted at the Lutjewad atmospheric station (53°24'13.5"N, 6°21'10.6"E). This 60 m-tall tower is located in the north of the Netherlands, on the Wadden Sea coast (Fig. 1). The station is part of the Integrated Carbon Observation System (ICOS) network, and continuously provides data on CO_2, CH_4 and CO mole fractions at 60 m height.

The surrounding area on land is mostly covered by intensive agriculture, including grazing land and production of

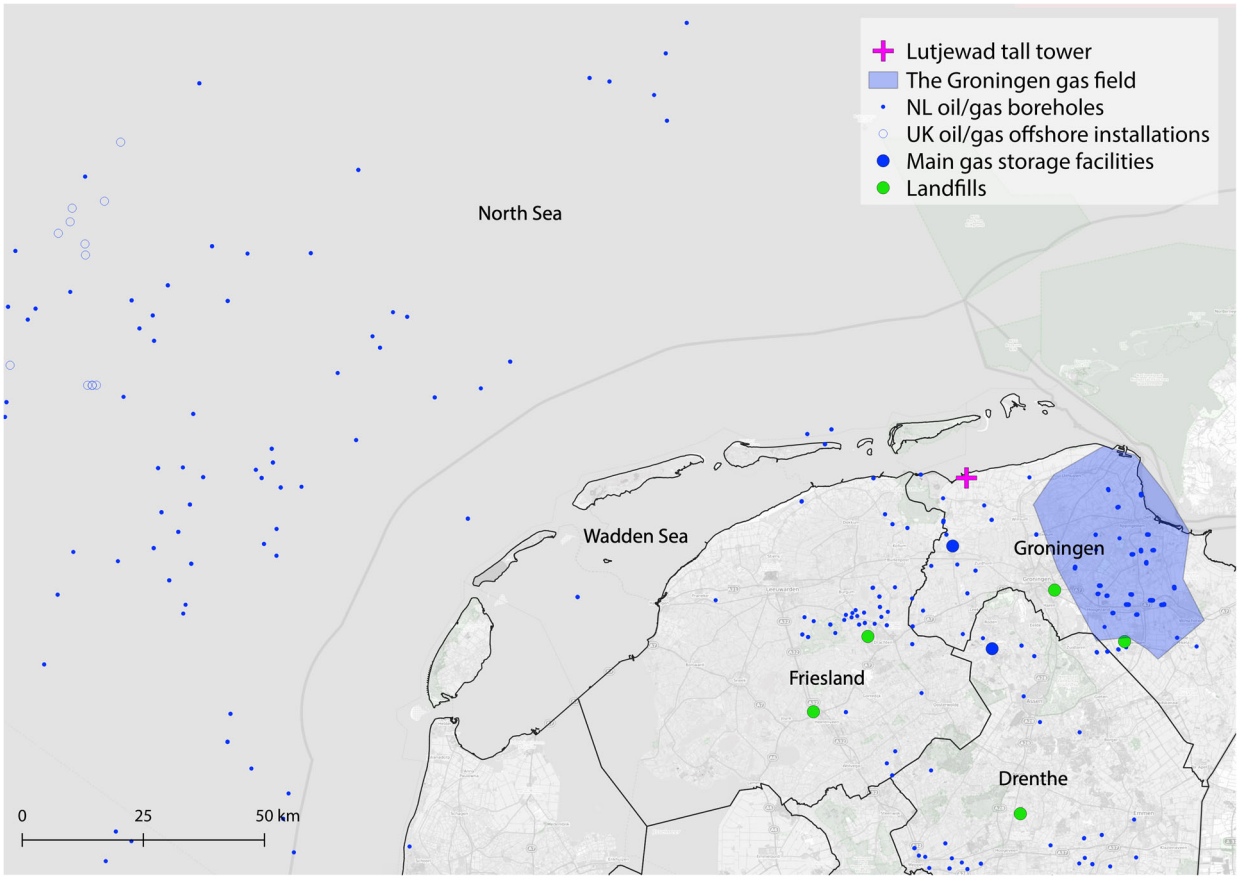

Fig. 1. Location of the measurement site (magenta cross) and potential on-shore and off-shore methane sources. Sources: https://www.openstreetmap.org, OSPAR Commission (2015), Vlek (2018), Ministerie van Economische Zaken, TNO (2018), and Stortplaatsen in Nederland (2019).

vegetables, mais and other cereals (Wageningen University & Research, 2015). The region has one of the highest livestock densities in Europe, among which a majority of bovines since the largest dairy farms in the Netherlands are in the province of Friesland (European Union, 1995; Fig. 1). The region is also characterised by the extraction of natural gas from sandstone layers at about 3 km depth. Locations of individual onshore boreholes are shown in Fig. 1. The Groningen gas field, the biggest natural gas reservoir of the Netherlands, is located east/southeast of Lutjewad at a distance of about 30 km (Fig. 1).

In the North Sea, between the Netherlands and the UK, a total of 445 platforms for oil and gas extraction are in operation (OSPAR Commission, 2015). They are mostly located in the west and northwest of Lutjewad (Fig. 1).

2.2. Measurements

2.2.1. Isotope ratio mass spectrometry system. The isotope measurement system is based on a continuous flow isotope ratio mass spectrometry (CF-IRMS) system. One IRMS instrument (Thermo Delta Plus XP, Thermo Fisher Scientific Inc., Germany) was used to measure alternatively ^{13}C-CO_2 and ^{2}H-H_2. Before injection into the mass spectrometer, CH_4 needs to be isolated from the other air components and converted to CO_2 or H_2. To extract the CH_4, ambient air is first pumped through magnesium perchlorate, a drying agent. Then, the dry air is sent through two successive cryogenic traps, cooled to $-120\,^{\circ}C$ and filled with HayeSep D in the center and glass beads on each end. The cooling is achieved by a Polycold compact cooler compressor (Brooks Automation Inc., USA), filled with coolant PT-30. The cold end is attached to a copper block on which the traps are mounted. The traps are kept under vacuum to avoid condensation of water and to allow a fast and precise temperature control of each of them. The methane is released by heating the traps to $-45\,^{\circ}C$, and then it is converted to CO_2 and H_2 in combustion and pyrolysis furnaces, at temperatures of 1150 and $1350\,^{\circ}C$, respectively. CO_2 is further purified on a gas chromatography (GC) column, at a temperature between 0 and $10\,^{\circ}C$. The

whole extraction process is illustrated in Fig. S1, and described in more detail in Röckmann et al. (2016). A picture of the extraction system installed at Lutjewad is shown in Fig. S2.

The fully automated system achieves one measurement of δ^{13}C- or δD-CH_4 every 20 min, together with the CH_4 mole fraction. Ambient air measurements were alternated with measurements of air from a reference cylinder. The cylinder contained air with 1974.0 ppb CH_4, and isotope values of $\delta^{13}C = -47.75 \pm 0.05‰$ vs V-PDB and $\delta D = -87.9 \pm 1.1‰$ vs V-SMOW, linked to a previous calibration against the international standard material at the Max Planck Institute for Biogeochemistry, Jena, Germany (Sperlich et al., 2016). After processing, the data resulted in time series for δ^{13}C-CH_4 and δD-CH_4 in ambient air, at a non-regular interval of 51 minutes on average.

CH_4 mole fractions were measured continuously by two CRDS (cavity ring-down spectrometry) instruments (model G2301 until 13/12/2016 followed by model G2401 since then, Picarro inc., CA, USA) connected to the same inlet as the IRMS. A set of instrument-specific empirical water vapor correction factors were used to derive CH_4 dry air mole fractions (Chen et al., 2010; Rella et al., 2013). For calibration of the G2301 CRDS we used working standard mixtures made in-house from dried ambient air and a suite of 5 primary standards (provided by the Earth System Research Laboratory (ESRL) of the National Oceanic and Atmospheric Administration (NOAA)) linked to the World Meteorological Organization (WMO) X2004 scale for CH_4. Together with the installation of the G2401 CRDS we replaced our calibration tanks by a suite of new ICOS standard mixtures prepared by the ICOS Central Analytical Laboratory (Jena, Germany) linked to the WMO X2004A scale for CH_4 for calibration. The total uncertainty of the CRDS $\chi(CH_4)$ was estimated to be 2 ppb. The measurements were made at 1 Hz; however, minute averaged values were used for the analyses. The measured $\chi(CH_4)$ from the IRMS were compared to these values. To do so, the time series were cut into subsets from 3 h to 8 days, according to maintenance breaks in the measurements. The average difference between the IRMS and CRDS $\chi(CH_4)$ values was calculated for each subset but only for $\chi(CH_4)$ <2250 ppb, because the values changed very rapidly during pollution events. If the average difference was larger than its standard deviation, it was considered a significant offset. The IRMS data were then corrected relatively to the CDRS values by applying this average difference. Corrections were finally applied to 62% of the data. They ranged from 2.17 to 112 ppb. Not every subset had a significant offset, and these $\chi(CH_4)$ differences were always very stable within each subset.

2.2.2. Meteorological data. Hourly measurements of wind speed and wind direction were used to interpret the methane time series. The meteorological data collected at Lutjewad at the different heights (7, 40 and 60 m above ground) were incomplete with missing data from 23 January 2017, onwards. Therefore, another dataset was used, from a nearby station of Lauwersoog (53°25'N 6°12'E), operated by The Royal Netherlands Meteorological Institute (KNMI). It is situated at about 10 km from the Lutjewad tall tower, and wind measurements at 10 m height are available for the entire measurement period. Both datasets show very similar wind characteristics despite the spatial and elevation difference.

2.3. Modelling

Using the atmospheric transport models CHIMERE and FLEXPART-COSMO, the time series of $\chi(CH_4)$, δ^{13}C-CH_4 and δD-CH_4 at the Lutjewad tall tower were modelled for the period of the measurements. CH_4 was treated as a non-reactive tracer in the models, considering the limited size of the domain and the correspondingly short residence time of the air compared to the lifetime of CH_4.

CHIMERE is a Eulerian regional chemistry-transport model (Menut et al., 2013; Mailler et al., 2017), here driven by the PYVAR system developped for forward comparison of model outputs and observations and variational inversions (Fortems-Cheiney et al., 2019). Forward simulations of CH_4 mole fractions were carried out at a horizontal resolution of 0.1° × 0.1° over a domain covering [43.6–55.6 N] in latitude and [5.0 W–12.0 E] in longitude. For the simulations, 29 vertical levels were used, reaching up to a top pressure of approximately 300 hPa. The meteorological data used to drive the model were taken from the European Centre for Medium-Range Weather Forecast (ECMWF) operational forecast product with a 10 km horizontal and 3-hour temporal resolution. The boundary and initial $\chi(CH_4)$ conditions were obtained from the analysis and forecasting system developed in the Monitoring Atmospheric Composition and Climate (MACC) project (Marécal et al., 2015). The version used for this study consists of 71 vertical levels, a horizontal resolution of 0.563° × 0.653°, and a temporal resolution of three hours. The meteorological products and the mole fraction fields were interpolated to the model domain both spatially and temporally by the PYVAR-CHIMERE system.

The FLEXPART-COSMO model is a version of FLEXPART (Pisso et al., 2019), an offline Lagrangian particle dispersion model (LPDM). This version uses the output of the mesoscale numerical weather prediction model COSMO (Baldauf et al., 2011) as the driving

Table 1. Initial $\delta^{13}C$ and δD values from literature used in the models for the different emission sectors (Szénási 2019). They are derived from signatures found in the cited studies. The range of values is reported in the brackets. Only the $\delta^{13}C$ value for fossil fuel emissions (bold) was modified from Szénási 2019 to better represent the emissions from this sector in the Netherlands.

Emission sector	δ13C-CH4 [o]	δD-CH4 [o]	Literature source
Agriculture	−68.0 [−70.6; −46.0]	−319 [−361; −295]	Uzaki et al., 1991; Levin et al., 1993; Tyler et al., 1997; Bréas et al., 2001; Bilek et al., 2001; Klevenhusen et al., 2010; Röckmann et al., 2016
Waste	−55 [−73.9; −45.5]	−293 [−312; −293]	Games and Hayes, 1976; Levin et al., 1993; Bergamaschi et al., 1998; Zazzeri et al., 2015; Röckmann et al., 2016
Extraction and distribution of fossil fuels & non-industrial combustion	**−40.0** [−66.4; −30.9]	−175 [−199; −175]	Levin et al., 1999; Lowry et al., 2001; Thielemann et al., 2004; Zazzeri et al., 2016; Röckmann et al., 2016
Other anthropogenic sources	−35.0 [−60; −9]	−175 [−175; −81]	Levin et al., 1999; Chanton et al., 2000; Nakagawa et al., 2005; Röckmann et al., 2016
Natural wetlands	−69 [−88.9; −51.5]	−330 [−358; −246]	Tyler et al., 1987; Smith et al., 2000; Galand et al., 2010; Happell et al., 1995; Martens et al., 1992; Bilek et al., 2001; Sugimoto and Fujita, 2006

meteorology. All meteorological fields are preserved on the original COSMO vertical grid, which strongly reduces uncertainties in the interpolation, compared to other versions of FLEXPART (Henne et al., 2016). For this study, FLEXPART-COSMO was driven by hourly output of the operational COSMO-7 analyses of the Swiss weather service MeteoSwiss at a horizontal resolution of 7 km × 7 km and with 60 vertical levels. 50,000 Lagrangian particles (air parcels) were released from the location of the monitoring site and its inlet at 60 m above surface every 3 hours and followed backwards in time over 4 days in order to derive sensitivity maps or footprints (Seibert and Frank, 2004).

The input anthropogenic CH_4 emissions were extracted from two gridded inventories for 2011: the EDGAR v4.3.2 (Janssens-Maenhout et al., 2017) and TNO-MACC III (Kuenen et al., 2014), with a horizontal resolution of approximately 11 km × 11 km and 7 km × 7 km, respectively. The CHIMERE simulations also used natural wetland emissions obtained from the ORCHIDEE-WET model (Ringeval et al., 2011) for 2009.

To be able to compare the two inventory outputs, the anthropogenic emission categories were grouped under the SNAP (Selected Nomenclature for Air Pollution) level-1 sectors (EEA (European Environment Agency), 2000). The emissions from five source categories were used to model the $\chi(CH_4)$ in CHIMERE: agriculture (SNAP 10), waste (SNAP 9), wetlands (SNAP 11), non-industrial combustion plants (SNAP 2), and production, extraction and distribution of fossil fuels (SNAP 5). The rest was characterised as" other" emission sources. In the results, SNAP 2 and SNAP 5 sectors were combined into one category for fossil fuel. The total simulated CH_4 mole fraction is a combination of the contribution of these emission sources and the background.

The $\delta^{13}C$-CH_4 and δD-CH_4 time series were calculated by both models based on the combination of the simulated CH_4 mole fractions for each source category and their associated isotopic signatures taken as one scalar per category, and were assigned based on previous studies (Table 1). The background isotopic signatures were obtained from the 3-hourly simulations of $\delta^{13}C$ and δD using the Laboratoire de Météorologie Dynamique (LMDz) model (Hourdin et al., 2006). The simulations followed the methods described by Thanwerdas et al. (2019). The values were taken from a model grid-cell above the North Atlantic. The background $\delta^{13}C$ values from this global model are on average −0.2‰ lower than the ones from the measurements. A corresponding correction was applied to the background isotopic composition to align it to the observations. The background δD values were also raised by 12‰, to better correspond to the observations. This correction is rather large, but corresponds to an offset between the scales of two groups of institutes - IMAU at Utrecht University, the Max Planck Institute for Chemistry in Mainz, Germany (MPIC), the National Institute for Water and Atmospheric Research in Wellington, New Zealand (NIWA) on the one hand and the University of California Irvine (UCI), Tohoku University (TU), the Institute of Arctic and Alpine Research (INSTAAR), and Pennsylvania State University (PSU) on the other hand - that was identified in an

international inter-comparison of isotope scales (Umezawa et al., 2018).

The total $\delta^{13}C$ and δD at each time point were computed in the following way:

$$\delta = \frac{1}{x(CH_4)_{tot}} \sum_{i}^{n=6} \delta_{s,i} * x(CH_4)_i$$

with δ_s being the source signatures defined in Table 1, for each emission sector i including the background.

2.4. Data analysis

The data were analysed using a Keeling plot approach (Keeling, 1961; Pataki et al., 2003), to obtain the source isotopic signatures of the recorded pollution events. This method is based on a mass balance equation considering addition of CH_4 from a single emission source (s) of a certain compound to a stable background (bg) in the measured sample (m):

$$\delta_m c_m = \delta_{bg} c_{bg} + \delta_s c_s$$

where δ is the isotopic value and c the mole fraction of the compound.

Re-arranging the equation, a linear relation can then be derived between $1/c_m$ and the measured isotopic signature (δ_m). The intercept corresponds to a maximum (infinite) concentration, that reflects the emission source isotopic signature δ_s:

$$\delta_m = \frac{c_{bg}}{c_m}(\delta_{bg} - \delta_s) + \delta_s$$

In the case of a mixture of several sources, δ_s may reflect the mean isotopic signature, weighted by emissions from the individual sources.

The Keeling plot method was applied in a similar way as in Röckmann et al. (2016), but with slight modifications. The moving time window had a width of 12 h of data and moved in steps of 1 h. At each step, $\chi(CH_4)$ values below the lower 10% percentile, and <2100 ppb, taken within a larger 24 h window were also included as background. A minimum number (n) of 5 points and a $\chi(CH_4)$ range of at least 200 ppb were used to select suitable datasets in these time windows. An orthogonal distance regression was then applied to determine the intercept of the $\delta_m : 1/c_m$ correlation and its uncertainty. Only linear fits with a standard error of the regression $s < 2.5‰$ were selected for further evaluation. This represents the typical distance between the data and the regression line. If this condition was not fulfilled, the window was narrowed by 1 h, until either $n < 5$ (rejected) or $s < 2.5‰$ (selected).

The signatures obtained were then filtered for those with a well-defined isotopic composition, indicating that the dataset can be fit assuming a source with a constant isotope signature. The following criteria was applied:

$$\sigma_{\text{intercept}} < \begin{cases} 1.5‰ & \text{for } \delta^{13}C \\ 30‰ & \text{for } \delta D \end{cases} \text{ and } \sigma_{\text{winddir.}} < 90^{\circ}$$

with $\sigma_{\text{intercept}}$ and $\sigma_{\text{winddir.}}$ being the standard deviation of the regression intercept and of the wind directions in the window. Applying these criteria filtered out 14% of the initial signatures from the moving window Keeling plot in total. The $\sigma_{\text{intercept}}$ threshold filters out more data than the one for the $\sigma_{\text{winddir.}}$.

In some cases, several regression intercepts were derived from the same pollution event, i.e. when a $\chi(CH_4)$ peak was longer than 12 h. In this case, they were averaged over the duration of the peak to obtain one source signature per pollution event.

3. Results

3.1. Overview

The complete dataset measured over 5 months is shown in Fig. 2. The gaps in the data are caused by technical failures.

The $\chi(CH_4)$ time series shows pronounced variability, compared with measurements from the Mace Head background station in Ireland made by the Advanced Global Atmospheric Gases Experiment (AGAGE, Prinn et al., 2008). In the first half of the period (until mid January 2017), CH_4 elevations were interrupted by periods when background values prevailed over longer periods. For example, the $\chi(CH_4)$ stayed stable and matched Mace Head values over a few days in the end of December 2016. The average $\chi(CH_4)$ measured at Mace Head was 1950 ± 39 ppb, which compares well with the observed background value of 1933 ± 11 ppb from Lutjewad (average of the lower 10% percentile of $\chi(CH_4)$).

The $\delta^{13}C$ time series can also be compared to measurements from flask samples taken at Mace Head, by the National Oceanic and Atmospheric Administration (NOAA; Dlugockenky et al., 2019; Fig. 2). No measurements are available for δD, but we expect δD values at Mace Head to match the background values from the Lutjewad measurements in a similar way as for $\delta^{13}C$. CH_4 elevations in the Lutjewad dataset are systematically accompanied by negative excursions of both $\delta^{13}C$ and δD values. The isotopic values reached down to $-51.8‰$ for $\delta^{13}C$ and $-147‰$ for δD, whereas the average background was -47.7 ± 0.21 and $-84.2 \pm 5.2‰$, respectively. The background from the measurements, calculated as the average of the 10% lower percentile of $\chi(CH_4)$, compares well with the average $\delta^{13}C$ of $-47.7 \pm 0.1‰$ at Mace Head during the time period.

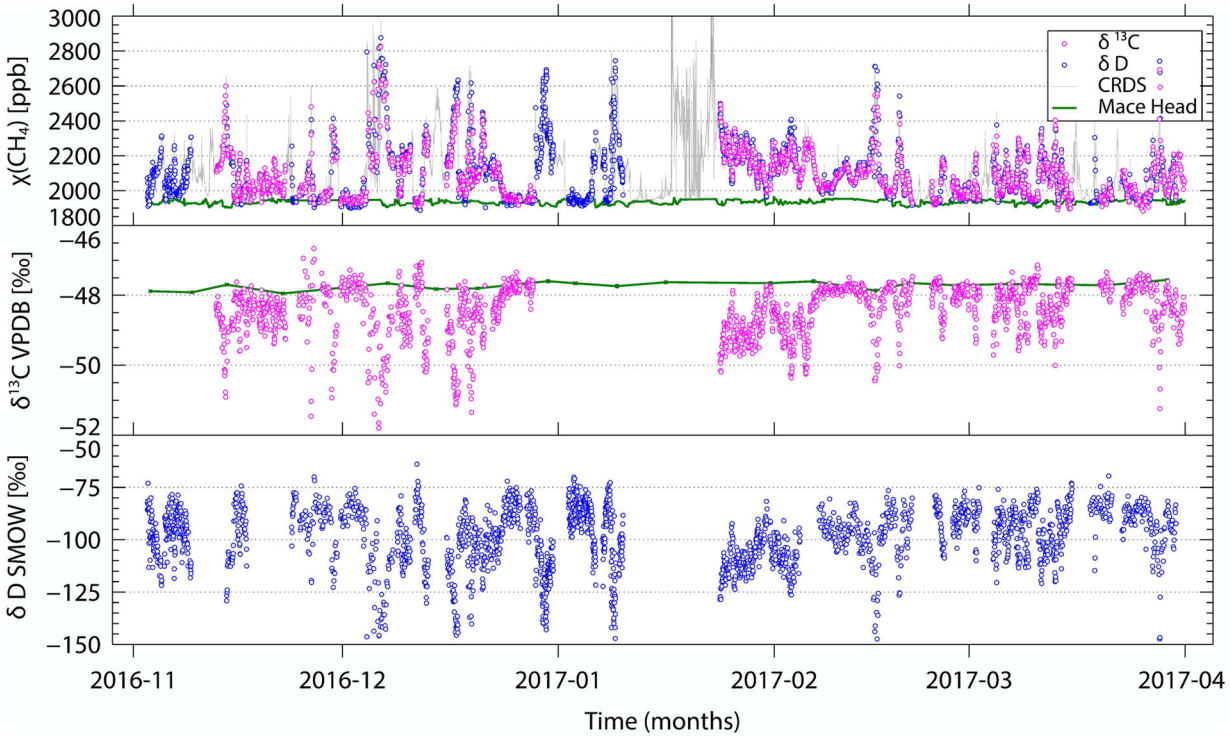

Fig. 2. Overview of the entire dataset, including corrections made on IRMS $\chi(CH_4)$ to match the CDRS records. The Mace Head $\delta^{13}C$-CH_4 data (Dlugockenky et al., 2019) was corrected by −0.11‰ according to the scale difference between the INSTAAR and the IMAU measurements evaluated in Umezawa et al. (2018).

In Fig. 3, the recorded methane and isotope data are plotted in wind roses. The main wind directions during the study period were from south-west (195° to 225°) and south-east (150°). A north-east to south-west line separates the land and sea. One can see that most of the pollution events originate from the land, and that periods with a pronounced northerly wind component were rare. The wind from the sea generally advects air with background $\chi(CH_4)$.

Accordingly, the background isotopic signatures are also observed during periods with north/north-west winds. Background isotope values are the high values for $\delta^{13}C$ and δD. The measured methane enhancements are mostly caused by isotopically depleted sources from the land, especially in the south, from which the lowest $\delta^{13}C$ and δD values were measured.

We also investigated the daytime-nighttime difference of mole fraction and isotope values (shown in Fig. S3). Background values of $\chi(CH_4)$, lower than 2000 ppb, are observed more often during the day than at night. Indeed, 35.5% of daytime $\chi(CH_4)$ records are lower than 2000 ppb, compared to only 30.5% nighttime. Small elevations in $\chi(CH_4)$ (lower than 2300 ppb) occur more during the night. Yet there is no clear distinction between daytime and nighttime for higher CH_4 elevations.

3.2. Model results

3.2.1. Time series. Modelled time series generated with CHIMERE and FLEXPART-COSMO are shown in Fig. 4(a,b). In general, the timing of the pollution events is in good agreement with the observations, and this is also true for the variations in the isotope signatures.

Figure S6 shows $\chi(CH_4)$, $\delta^{13}C$ and δD-CH_4 histograms from the measurements and model results. Correlation plots between model and observations are also provided in the supplementary material (Fig. S7). According to the distribution of CH_4 mole fractions in Fig. S6(a), higher $\chi(CH_4)$ elevations are less present in the simulation results compared to the measurements, especially from CHIMERE. This variation is likely due to the comparison between hourly averages of instant measurements at a certain location and values over a larger grid cell provided by the model. The general $\chi(CH_4)$ distribution is better reproduced with FLEXPART-COSMO (Fig. S7(a)). A higher proportion of $\chi(CH_4)$ values between 2050 and 2100 ppb was computed with CHIMERE, mostly from an overestimation of the mole fractions in March 2017 (Fig. 4(a,b)).

The difference between model results and observations at higher mole fractions also affects the isotopic composition. Figure 6(a,b) show that the modelled isotopic

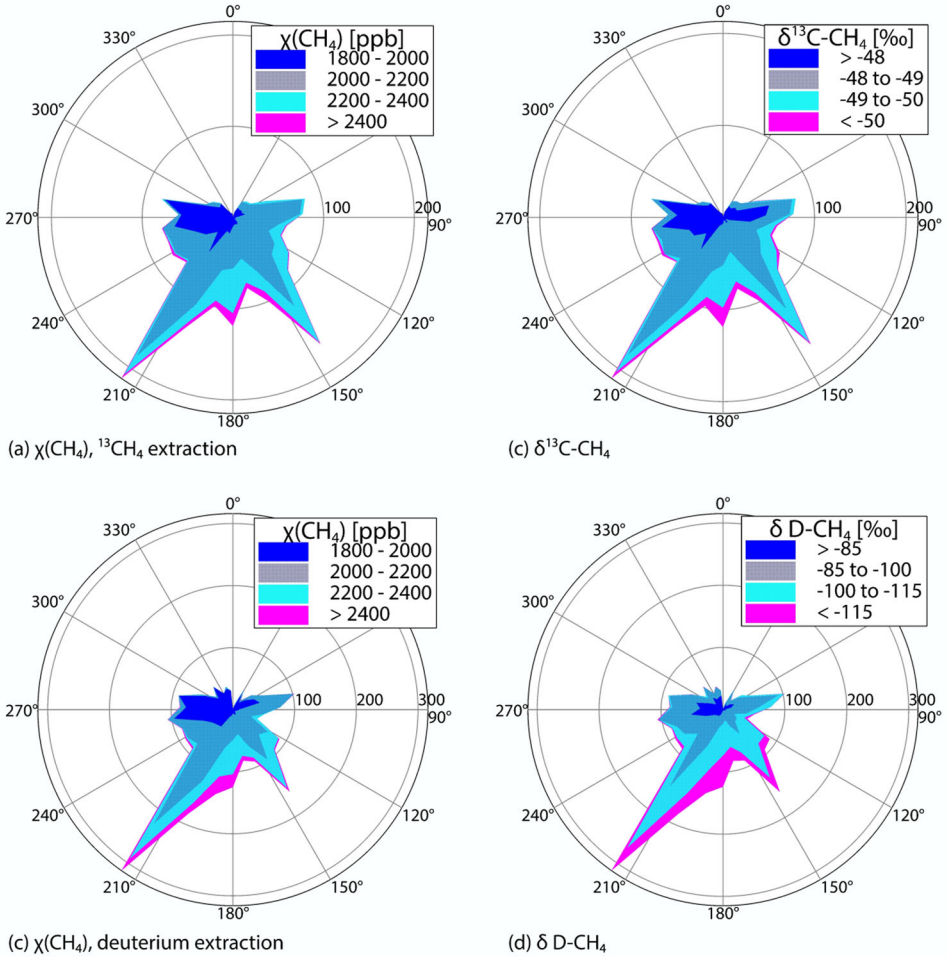

Fig. 3. Wind rose diagrams of $\chi(CH_4)$, $\delta^{13}C\text{-}CH_4$, and $\delta D\text{-}CH_4$, in number of records with respect to the wind direction. The North is set at 0°, as for all the direction angles throughout the article.

signatures are often less depleted than the measured ones, especially for the FLEXPART-COSMO simulations. In general, the differences are also higher for δD, but the time series of this isotope also have higher uncertainties.

There is no clear difference between the use of the TNO-MACC III inventory and the EDGAR v.4.3.2 inventory regarding the overall distribution of $\chi(CH_4)$ and $\delta D\text{-}CH_4$. For $\delta^{13}C\text{-}CH_4$, using the TNO-MACC III inventory leads to more enriched values than with EDGAR v.4.3.2 (Fig. 6(a)).

3.2.2. Source partitioning. The contributions from each CH_4 source category as computed with the CHIMERE model are presented in Table 2. The dominant source is the agriculture sector, with a contribution close to 60%. The second most important source is waste, followed by emissions from fossil fuels. Other sources and wetlands contribute less than 10%. Both inventories agree on the ranking of the different sources. The largest difference is in the share of the fossil fuel contribution. When TNO-MACC III inventory is used, the contribution of fossil sources to the modelled CH_4 elevations is about 45% larger than for EDGAR v4.3.2.

3.3. Source signatures

From the Keeling plots of the entire observations dataset (Fig. S4(a,b)), the total averaged source signatures are $-59.55 \pm 0.13‰$ and $-287.2 \pm 1.4‰$ for $\delta^{13}C$- and $\delta D\text{-}CH_4$, respectively. These values are typical for microbial (including waste) methane emissions, in agreement with the source attribution from the model.

The results from the moving window Keeling plots also show a prevalence of isotopically depleted sources: the mean isotope signatures of the evaluated peaks are respectively $-60.3 \pm 3.1‰$ and $-286.3 \pm 27.5‰$ for $\delta^{13}C$ and δD. These values agree within the uncertainties with the Keeling plot intercepts made with all points of the

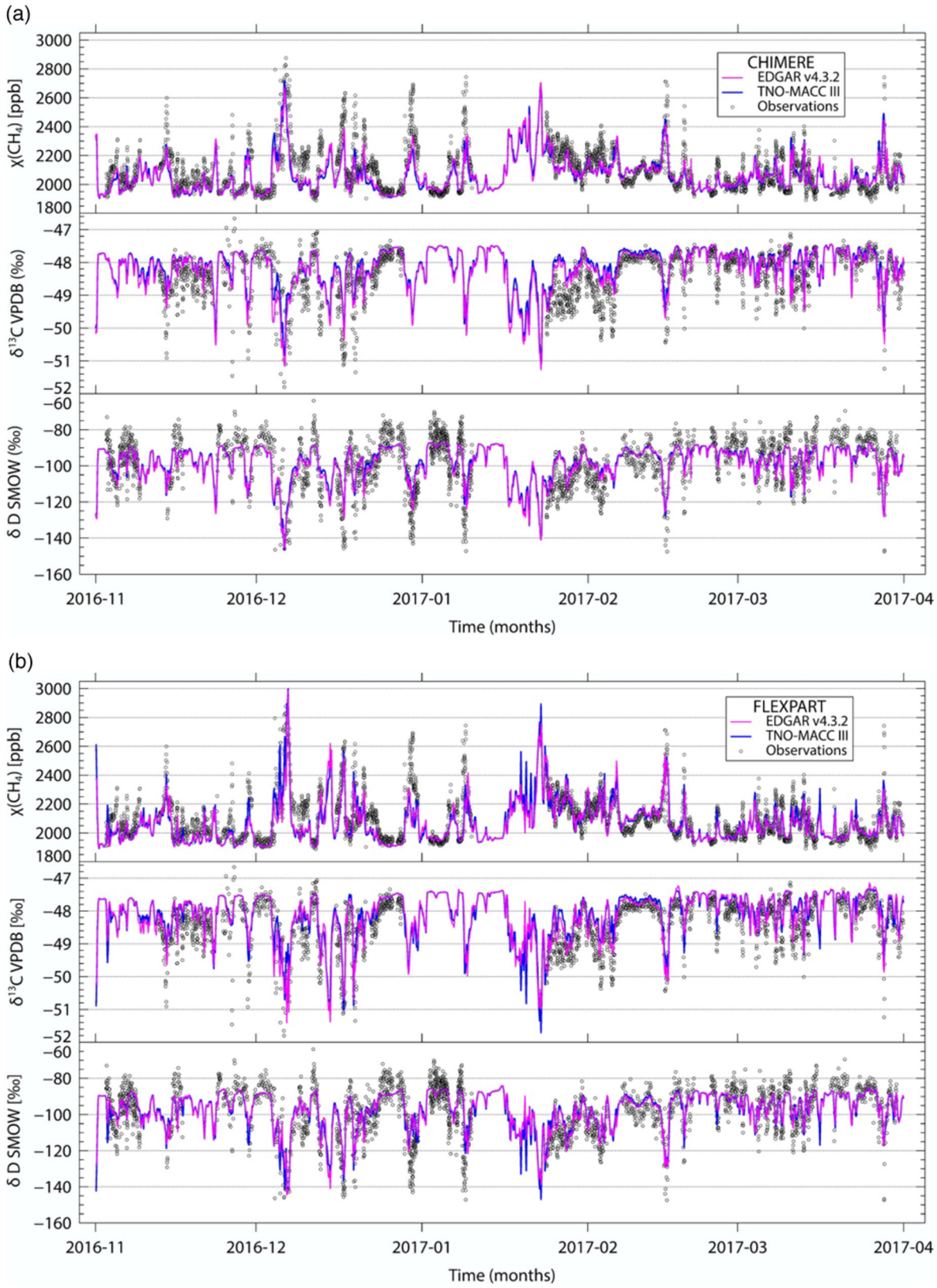

Fig. 4. Model results from CHIMERE and FLEXPART-COSMO, using two emission inventories.

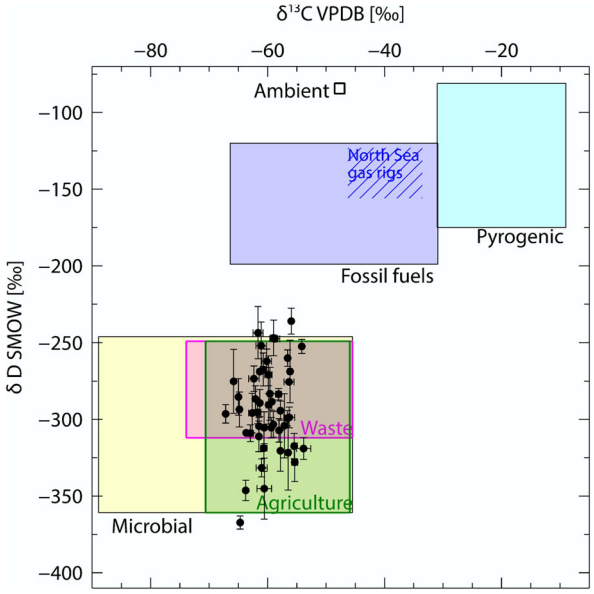

Fig. 5. δ^{13}C- and δD-CH_4 source signatures, derived with the moving window Keeling plot approach (black dots). The background CH_4 isotopic composition corresponds to the 10th lower percentile of the $\chi(CH_4)$ in this study's dataset. Colored areas indicate typical isotope signatures for CH_4 (referred in Table 1 and partially from unpublished measurements of biogenic sources made in the Netherlands). The δ^{13}C of the North Sea gas rigs is between −32 and −45‰, from Hitchman, S. P. (1989), Cain et al. (2017) and Riddick et al. (2019).

dataset. Figure 5 compares our observed atmospheric average isotopic signatures to typical ranges for specific sources in previous studies. Almost all of the source signatures from Lutjewad fall within the 'Agriculture' and 'Waste' areas, that are anthropogenic emissions of 'Microbial' origins. The δD and δ^{13}C spread suggests variations in the contribution from thermogenic sources. The reported isotopic composition of North Sea and on-shore Dutch natural gas lie in the upper range of thermogenic ^{13}C (^{13}C-$CH_4 = -33 \pm 1$‰ reported by Cain et al. (2017), ^{13}C-$CH_4 = -43.7$‰ reported by Riddick et al. (2019), and δD-$CH_4 = -158$ to -121‰ reported by (Hitchman, S. P. 1989). This already shows that the observed methane elevations contain only relatively small fractions of thermogenic methane.

Histograms of the peak source signatures are shown in Fig. 6. The source signatures from modelled time series also fall in the range of biogenic emissions. Using the TNO-MACC III inventory leads to more enriched source signatures because of its higher proportion of fossil fuel emissions.

3.4. Individual pollution events

Two periods were selected to analyse individual pollution events in more detail, together with results from the CHIMERE model. The Keeling plots for a moving time window were also applied to the CHIMERE results, using the same criteria as for the observations. The first subset is from the 16–21 December 2016 (Fig. 7) and the second from the 10–16 March 2017 (Fig. 8).

In the first subset (16–21 December 2016), there are three pollution events of relatively high magnitudes. They are labelled in Fig. 7 as 1 (December 17), 2 (December 19), and 3 (December 21). The elevations are also seen in the CHIMERE model results, albeit with lower magnitude, likely due to the rather coarse resolution of this model. Wind directions varied considerably during this time period: 219 ± 30°, 149 ± 32°, and 179 ± 21°N, respectively for each event (Fig. 7). The isotope source signatures of the first two events are between −64.3 and −62.6‰ for δ^{13}C and between −323 and −297‰ for δD in the measurements, but increase to −55.1‰ for δ^{13}C and −233‰ for δD during the third event. The model captures the isotope signatures of the three events relatively well when the EDGAR inventory is used. The TNO-MACC III inventory shows an increase in fossil fuel-related emissions on December 19th and 20th, and a corresponding δ^{13}C enrichment. For event 2, this is not confirmed by the measured δ^{13}C values, which indicate a prevalent biogenic source. For event 3, the measured δD source isotopic signature reaches -232 ± 6.7‰, the highest value derived from this dataset. In Fig. 5, this point clearly falls outside typical isotope signatures for biogenic sources and waste. The associated δ^{13}C-CH_4 is -55.1 ± 0.71‰. It does not correspond to the typical North Sea gas source signature, which is usually more enriched (Fig. 5). Yet it is also among the highest δ^{13}C values derived from this dataset. This strongly suggests that this pollution event contained a higher proportion of CH_4 from non-biogenic sources on land (because of a southern wind). Event 3 was not elevated enough in the model using TNO-MACC III to allow calculation of the isotope source signatures (selection criteria (see section 2.4) were not fulfilled). Both emission inventories show a higher proportion of wetland emissions, combined with a relatively large fossil fuel contribution in EDGAR v4.3.2. This also caused higher signatures for this event from the model results, but not as much as in the measurements, likely because of the additional contribution of isotopically depleted CH_4 from wetlands. The inventories locate wetlands along the North Sea coast of the Netherlands, but in this case the emissions are not confirmed by the measurements.

In the second subset (10–16 March 2017), four pollution events were recorded, also labelled in Fig. 8. The two events on March 11th (4 & 5) closely follow each other, the second one showing a smaller elevation than the first. The model reproduces well events 4, 6 and 7,

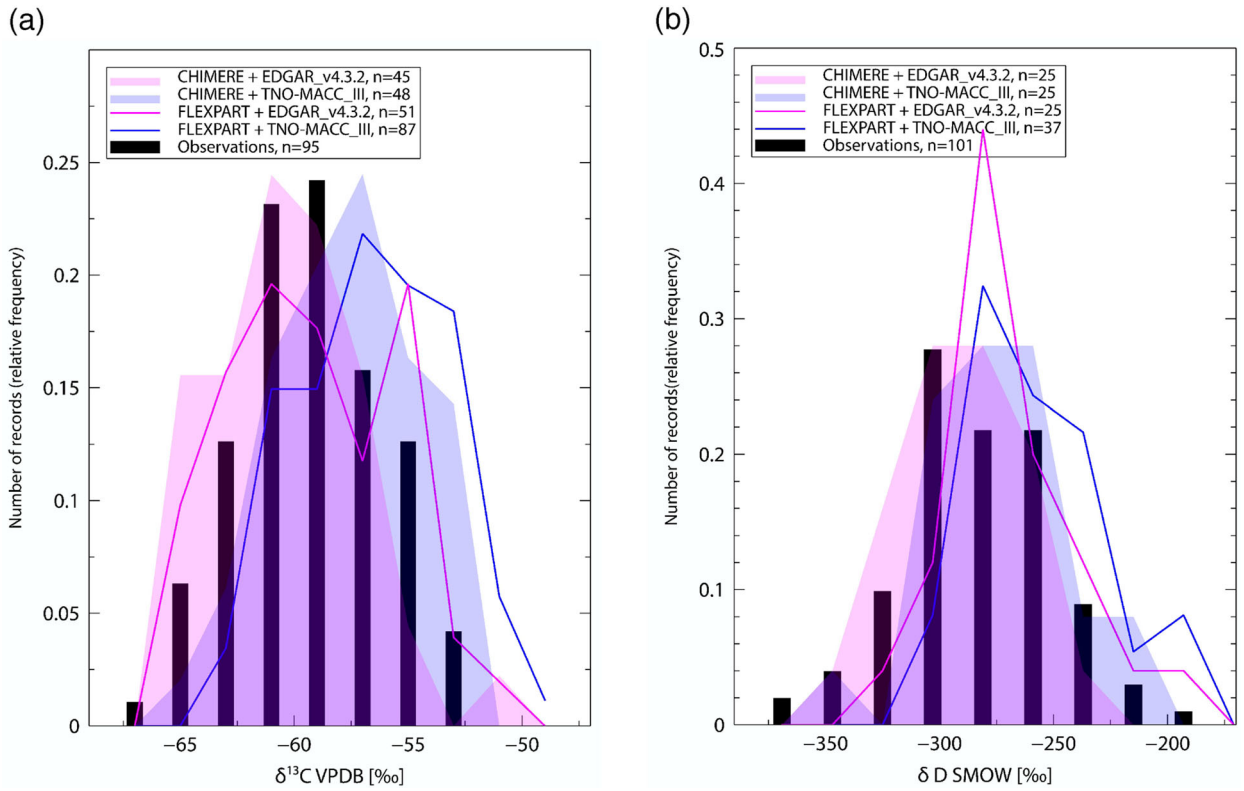

Fig. 6. Frequency distribution of the $\delta^{13}C$ and δD source signatures derived from the moving window Keeling plot approach applied to the observation and modelled time series, interpolated linearly to the measurement times. Signatures from the same peak were averaged to give one value per pollution event.

but shows another pollution event before event 4, which was not measured. Also, the small $\chi(CH_4)$ elevation of event 5 is not present in the model simulations, so no Keeling plot intercept could be derived. Event 4 is associated with a sharp switch in wind direction: from northwest background air to southeast land emissions. It is characterised by a higher contribution from fossil fuel sources, modelled with both TNO-MACC III and EDGAR v4.3.2 inventories. Yet this contribution is overestimated by TNO-MACC III. The corresponding $\delta^{13}C$ and δD signatures are still low, because biogenic emissions are still the prominent source. Even though the wind direction stays at $132 \pm 14°$, the measured isotope source signatures clearly decrease further for event 5. This qualitatively confirms the decrease in the fossil fuel contribution for the model runs using the EDGAR v4.3.2 inventory between these two events. Event 7 (morning of March 14, Fig. 8) was not elevated enough in the model to obtain an isotope source signatures from the Keeling plots. The source partitioning from both inventories still suggests a higher contribution from fossil fuel sources during this event. This is confirmed by the higher δD during event 7 compared to event 6 from the measurements. Yet, the measured $\delta^{13}C$ decreases slightly. This anti-correlation between $\delta^{13}C$ and δD is rarely observed in the time series and cannot be explained with the assignment of fixed isotope signatures used in our evaluation. There is a shift in the wind direction during event 6: from $123 \pm 5°$N to $235 \pm 18°$N. This suggests a change in the pollution source, yet the signatures from the observations remain stable.

4. Discussion & conclusion

4.1. Spatial and temporal variability

There is a seasonal cycle in the background methane mole fractions in the northern hemisphere due to the higher abundance of OH radicals in the summer (Dlugokencky et al., 2011). The dataset presented here was taken over the fall and winter months and is not strongly affected by this annual variability. The background $\chi(CH_4)$ measured at Mace Head were stable over the 5 months of measurements, and were in good agreement with the measured values when the wind was coming from the west.

Diurnal variability is to a large degree driven by the accumulation of compounds from surface emissions during the night, and more vertical mixing during the day.

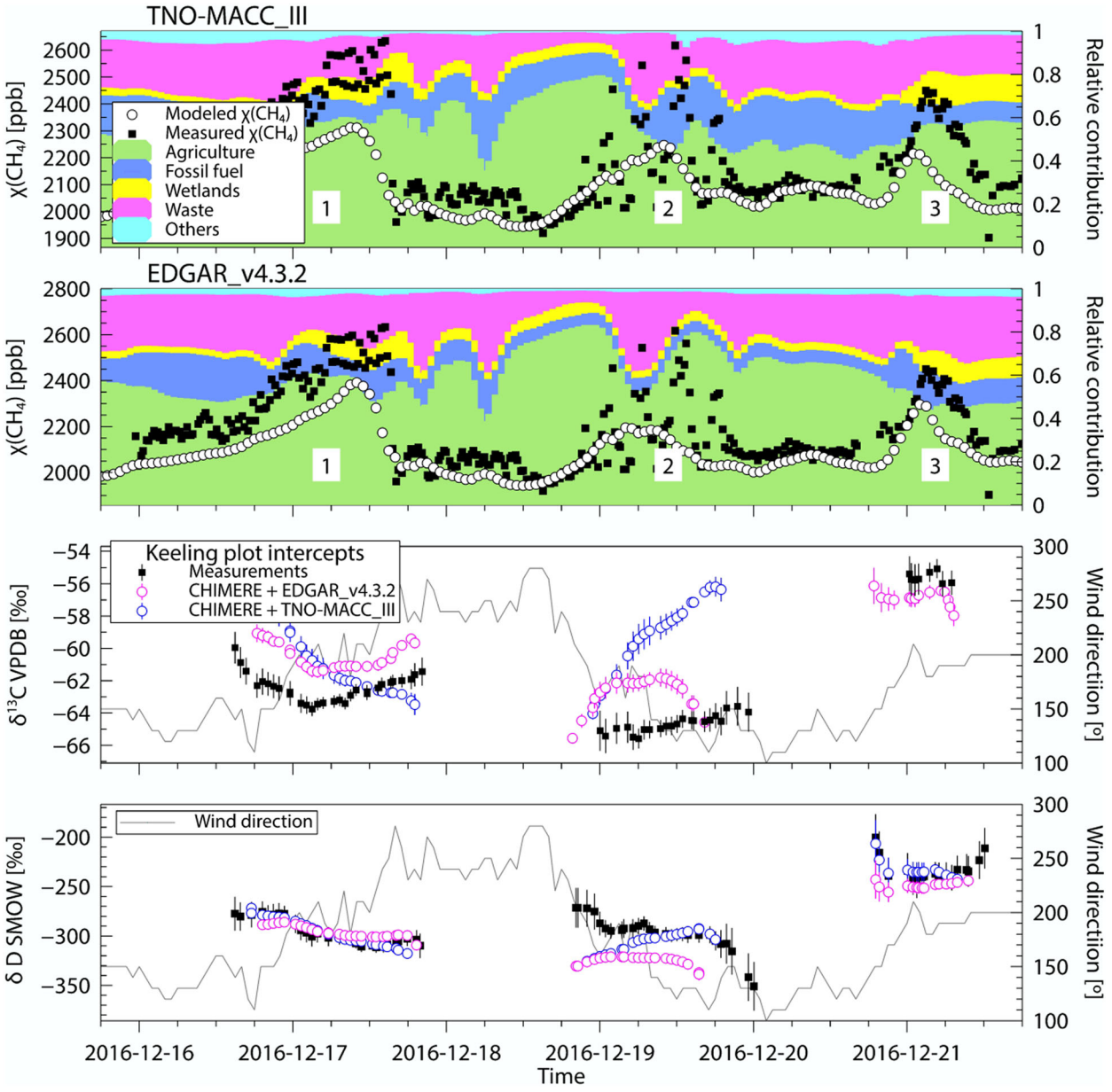

Fig. 7. December 16 to 21 subset. The upper panels show $\chi(CH_4)$ time series with an average time resolution of 51 min for the observations and 1 h for the model (left axis), with the modelled source partitioning (right axis). The lower panels show source signatures resulting from the moving window Keeling plot (left axis) with the recorded wind directions (right axis).

Table 2. Overall contribution from each source type to $\chi(CH_4)$ from CHIMERE, in [%] $\pm 1\sigma$.

Source sector	TNO-MACC III	EDGAR v4.3.2
Agriculture	58.6 ± 12.0	62.3 ± 12.9
Fossil fuels	14.5 ± 7.9	10.7 ± 5.9
Waste	17.9 ± 7.8	19.0 ± 9.6
Wetlands	6.1 ± 3.5	5.7 ± 2.7
Others	3.0 ± 2.5	2.3 ± 1.0

During the two episodes presented in detail in the results section, the highest $\chi(CH_4)$ elevations were recorded in the beginning of the day. The nighttime accumulation is therefore visible in the measurements almost everyday, at least during the winter months.

On March 10, no elevation was recorded: the average $\chi(CH_4)$ was 1954 ± 13 ppb from 00:00 to 22:00, which is close to the the overall background of 1933 ± 11 ppb (section 3.1), and the values observed at Mace Head. This

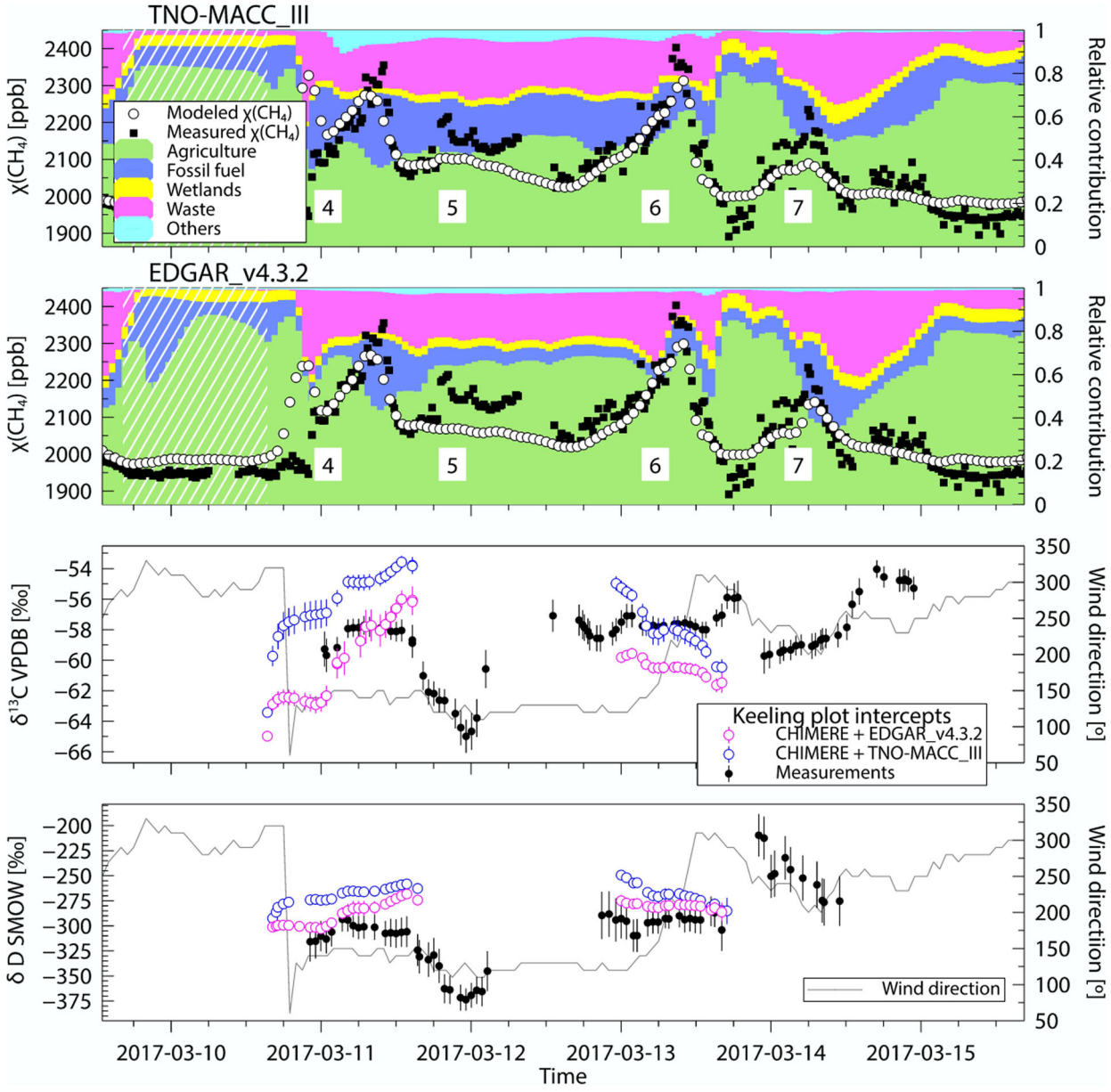

Fig. 8. March 10 to 15 subset. The upper panels show $\chi(CH_4)$ time series with an average time resolution of 51 min for the observations and 1 h for the model (left axis), with the modelled source partitioning (right axis). The lower panels show source signatures resulting from the moving window Keeling plot (left axis) with the recorded wind directions (right axis). The white hatching shows stable background $\chi(CH_4)$ advected by northern winds.

part is highlighted in Fig. 8 (white hatching). The wind in the period March 9, 16:00 to March 10, 18:00 was from west/northwest ($300 \pm 14°$N), bringing background air from the sea. In general, background values in the dataset were mostly advected by winds from 250 to 360°N.

Variations in wind direction on longer time scales also affect the results: southerly to southwesterly winds were prominent in December and January, whereas easterly winds, from 80 to 100°N, almost never occurred. Southwesterly winds advected the highest mole fractions of the dataset (Fig. 3(c,d)), corresponding to important biogenic CH_4 sources. They can be attributed to agriculture (mainly cattle farming), waste management, and to a smaller extent, wetlands (Fig. 7, event 1). Easterly winds did not bring air with very high $\chi(CH_4)$, but some of the elevations were associated with a significantly higher $\delta^{13}C$ (Fig. S5). Emissions from the Groningen gas field can potentially be the cause of this enrichment. Both

Table 3. Comparison of the averaged source signatures obtained from the Cabauw and Lutjewad time series. The values (y-intercept in [‰] $\pm 1\sigma$) are obtained from a weighted orthogonal distance regression (ODR) minimising the sum of squared weighted orthogonal distances of all the data points to the fitted curve.

Averaged source signatures	Cabauw (Röckmann et al., 2016)	Lutjewad (this study)
δ^{13}C vs V-PDB	-60.8 ± 0.2	-59.5 ± 0.1
δD vs V-SMOW	-298 ± 1	-287 ± 1

EDGAR v4.3.2 and TNO-MACC III inventories report large fossil fuel emissions in northwest Germany, which may have also contributed. There is no clear evidence, however, of this higher fossil fuel contribution from the δD results. Fewer δD signatures were obtained from easterly winds. Indeed, the selection criteria for the moving window Keeling plots were rarely fulfilled due to the low CH_4 elevations combined with the higher measurement uncertainties for this isotope signature.

4.2. Source identification

The resulting source isotopic signatures clearly confirms that at Lutjewad station the dominant sources are microbial. This includes emissions from the waste sector, but these source categories are not easy to disentangle since the source isotopic signatures partially overlap (Fig. 5). The emission sources that characterise the area are regional human activities such as cattle farming and waste management. The isotopic analysis gives a consistent interpretation of the methane source contributions, and is confirmed by the modelling exercise.

From November 2014 to March 2015, similar measurements were performed at the Cabauw tall tower site, in central Netherlands (Röckmann et al., 2016). The resulting source signatures derived from the entire datasets are compared in Table 3. Both δ^{13}C- and δD- CH_4 values point towards biogenic emissions, but are significantly different. The reasons might be a slightly larger contribution from enriched sources in the Lutjewad region, such as fossil fuel related emissions from the Groningen gas field and the German Ruhr area. Another possible explanation is that source signatures from biogenic emissions might vary slightly depending on the region. A potential seasonal effect is excluded, as both measurements were performed through the winter.

The presence of off-shore oil and gas platforms in the North Sea, in the northwest direction from Lutjewad did not lead to advection of thermogenic methane that could be detected on the Dutch coast. In contrast, the northwest wind transported mainly background air to our measurement station, and at higher wind speeds, supported by $\chi(CH_4)$ measurements at Mace Head. This is likely due to the large distance between the off-shore platforms and the coast. Yacovitch et al. (2018) suggested a larger contribution of CH_4 venting from off-shore facilities to the total Dutch oil and gas emissions than the one reported in the inventories. However, low emission rates were derived by Riddick et al. (2019), from measurements at 8 oil and gas platforms in the UK. Cain et al. (2017) also detected methane enhancements over UK gas rigs. The broad methane plume detected by Yacovitch et al. (2018) on 1 September 2016 could reasonably come from these installations. Measurements at closer distances from Dutch off-shore platforms, and at different times of the year are therefore required to better detect the isotopic composition of these emissions.

One pollution event with a larger contribution from fossil fuel sources was identified on 21 December 2016 (Fig. 7, event 3), coming from south of Lutjewad. The cause could be the two natural gas storage facilities that are in this direction. The isotopic enrichment was partially confirmed by the CHIMERE results. In the EDGAR v4.3.2 inventory, the fossil fuel emissions increased, but also the wetland contribution, which is characterised by an isotopically depleted CH_4. Wetland sources from the ORCHIDEE-WET model are located both in the central Netherlands and along the North Sea coast from Amsterdam to the North of France. But for this specific event, a larger influence from wetlands is not confirmed by the observations.

The modelled source contributions do not always agree with the isotopic measurements (Figs. 7 and 8). However, uncertainties remain in the range of signatures assigned to one source. The consequences will be discussed in the next section.

4.3. Model performance

The model time series agree well with the observations regarding the timing of the pollution events (Fig. 4). The measurements of $\chi(CH_4)$ show in general higher elevations, and consequently more depleted isotopic signatures. In the model, CH_4 mole fractions are averaged per hour, and therefore are always smoothed compared to measurement data. The time series from FLEXPART-COSMO correlate better with the measured mole fractions than

Table 4. Comparison of the averaged source signatures from measurements and models. They correspond to the Keeling plot intercepts using all data. The values (y-intercept in [‰] ± 1σ) are obtained from a weighted orthogonal distance regression (ODR) minimising the sum of squared weighted orthogonal distances of all the data points to the fitted curve.

	Obervations	CHIMERE	FLEXPART-COSMO	Inventory
δ^{13}C vs V-PDB	−59.5 ± 0.1	−57.2 ± 0.2	−57.2 ± 0.1	EDGAR v4.3.2
		−55.2 ± 0.2	−55.4 ± 0.1	TNO-MACC III
δD vs V-SMOW	−287 ± 1	−266 ± 2	−253 ± 1	EDGAR v4.3.2
		−254 ± 2	−249 ± 2	TNO-MACC III

CHIMERE, which may be explained by its higher horizontal resolution.

Although the results are generally similar when using the two different inventories (Fig. 4), the relative source contributions do change when another inventory is used. The main difference is in the contribution from fossil fuel sources, estimated as 14.5% when using the TNO-MACC III inventory, whereas it is only 10.7% when using the EDGAR v4.3.2 (Table 2). Simulations using the TNO-MACC III inventory overestimate the average source signature by 2 and 12‰ more for δ^{13}C and δD respectively, than simulations with EDGAR v4.3.2 (Table 4, Fig. 6). This is in line with the higher fossil fuel emissions in TNO-MACC III. The average source signature and the ones of individual events from the CHIMERE model results are closer to the observations when using EDGAR v4.3.2 (Table 2, Figs. 7 and 8).

Table 4 shows the average source signatures resulting from the Keeling plot of the entire dataset. The source signatures are overestimated when using both models, with both inventories. The best agreement for the average source signatures is with the CHIMERE results using the EDGAR v4.3.2 inventory. Wetland CH_4 emissions were not taken into account in FLEXPART-COSMO, which explains the relative enrichment in δ^{13}C compared to the CHIMERE results. If the wetland emissions are neglected in CHIMERE, the average source signature would change by +0.7 and +7‰ respectively for δ^{13}C and δD. Taking these emissions into account could significantly improve the agreement between the results from FLEXPART-COSMO and the observations.

The input isotopic signatures for the model are based on previous measurements reported in the literature. In the case of δ^{13}C, the numerous measurements reported for North Sea gas (Hitchman, S. P. 1989; Zazzeri et al., 2015; Cain et al., 2017; Riddick et al., 2019) allowed to adapt the fossil fuel emission source signature to the study location. A value of −40‰ was chosen for this category. Initial model calculations used with the original fossil fuel δ^{13}C of −47‰ as input to CHIMERE and FLEXPART-COSMO. The variability in the δ^{13}C observations was then not well reproduced by the model results, and the overall source signature was underestimated. Another test using a value of −33‰ was made with CHIMERE to represent only the most enriched North Sea gas emissions, and resulted in an overestimation of δ^{13}C compared to the measurements. This confirms the geographical dependency in the isotopic signature of fossil fuel CH_4 emissions.

Further sensitivity studies were performed to evaluate the origin of the mismatch in the average isotopic signature between observations and model. Only changes in the agriculture, waste and fossil fuel source signatures have a significant effect on the average, because they represent the largest shares of emissions. Regarding the fossil fuel signature, it is well constrained by previous measurements, as described in the previous paragraph. In order to match the observed overall Keeling plot intercept, δ^{13}C and δD source signatures in the CHIMERE model using EDGAR v4.3.2 emissions would need to be lowered to −72 and −349‰ for agriculture and −58 and −313‰ for waste, respectively. Using the TNO-MACC III inventory would imply even lower values for agriculture and waste. Within these categories, such depleted isotope signatures are not fully excluded, but highly unlikely based on values published in the literature. It is therefore unlikely that the differences can be attributed only to uncertainties in the assigned isotope signatures. Thus, our semi-continuous isotope measurements provide evidence for lower contributions from fossil sources compared to what is included in the inventories. A more comprehensive evaluation of source contributions using the same parametrisation of CHIMERE is currently in preparation (by B. Szénási).

Röckmann et al. (2016) assessed that fossil fuel related emissions were likely overestimated in the previous version of EDGAR v4.2 and these emissions have been significantly reduced in version EDGAR v4.3.2 used for this study. The results presented here demonstrate that this adjustment in the fossil fuel contribution leads to better agreement with the isotope measurements. However, the source partitioning in the inventory likely needs to be adjusted further.

4.4. Future investigations

Reported source signatures in the literature are much less numerous for δD-CH_4 than $\delta^{13}C$, and the input δD-CH_4 values for the different sources in the models are more uncertain. In this study, we observed a correlation between $\delta^{13}C$ and δD signatures, with a $\delta^{13}C$: δD slope of about 10 ‰/‰. However, this situation is specific to the Netherlands, as the thermogenic sources are particularly enriched (Fig. 5). In regions where fossil sources have lower $\delta^{13}C$ values than in the Netherlands, measurements of δD-CH_4 become crucial for source attribution. In general, more measurements of $\delta^{13}C$ and δD-CH_4 from the various sources would be valuable to better constrain the isotopic signatures used as input to the models, i.e. by taking into account potential seasonal and geographical variations within source categories.

The combination of isotope measurements with model data is particularly valuable for assessing the accuracy of emission inventories. In our study, the average isotopic signatures do not precisely match the measurements, but still confirm the predominance of biogenic emissions, which is expected in the Netherlands. The source contributions obtained from the CHIMERE model show that for some pollution events the modelled source attribution is supported by the measured isotope changes, but for others not. This demonstrates the power of the high temporal resolution isotope time series that can be obtained with an IRMS system operating at various locations. In the future, measurements of high-frequency $\delta^{13}C$ and δD at several locations and other countries, would better constrain the emissions on a larger scale. Current challenges lie in the technical complexity of the measurements and high quality logistics required to perform these measurements. They are the limiting factors for conducting similar studies in more remote and under-studied regions.

Data availability statement

The data that support the findings of this study are openly available in mamenoud/CH4-Lutjewad-2016-2017: First release (Version v1.0.0) at http://doi.org/10.5281/zenodo.3970888.

Disclosure statement

No potential conflict of interest was reported by the authors.

Supplemental data

Supplemental data for this article can be accessed **here**

Acknowledgements

We specially thank Bert Kers and Marcel de Vries at CIO for the technical support they provided during the measurements at Lutjewad.

Funding

This work was supported by the ITN project Methane goes Mobile – Measurements and Modelling ($MEMO^2$; https://h2020-memo2.eu/). This project has received funding from the European Union's Horizon 2020 research and innovation programme under the Marie Sklodowska-Curie grant agreement No 722479. AGAGE is supported principally by NASA (USA) grants to MIT and SIO, and also by: BEIS (UK) and NOAA (USA) grants to Bristol University; CSIRO and BoM (Australia): FOEN grants to Empa (Switzerland); NILU (Norway); SNU (Korea); CMA (China); NIES (Japan); and Urbino University (Italy).

References

Baldauf, M., Seifert, A., Förstner, J., Majewski, D., Raschendorfer, M. and co-authors. 2011. Operational convective-scale numerical weather prediction with the COSMO model: description and sensitivities. *Mon. Weather Rev. 139*, 3887–3905. doi:10.1175/MWR-D-10-05013.1

Beck, V., Chen, H., Gerbig, C., Bergamaschi, P., Bruhwiler, L. and co-authors. 2012. Methane airborne measurements and comparison to global models during BARCA: methane in the Amazon during BARCA. *J. Geophys. Res. 117*, 15310. doi:10.1029/2011JD017345

Bergamaschi, P., Frankenberg, C., Meirink, J. F., Krol, M., Villani, M. G. and co-authors. 2009. Inverse modeling of global and regional CH_4 emissions using SCIAMACHY satellite retrievals. *J. Geophys. Res. 114*, 301.

Bergamaschi, P., Lubina, C., Königstedt, R., Fischer, H., Veltkamp, A. C. and co-authors. 1998. Stable isotopic signatures (^{13}C,D) of methane from European landfill sites. *J. Geophys. Res. 103*, 8251–8265. doi:10.1029/98JD00105

Bergamaschi, P., Karstens, U., Manning, A. J., Saunois, M., Tsuruta, A. and co-authors. 2018. Inverse modelling of European CH_4 emissions during 2006–2012 using different inverse models and reassessed atmospheric observations. *Atmos. Chem. Phys. 18*, 901–920. doi:10.5194/acp-18-901-2018

Bilek, R. S., Tyler, S. C., Kurihara, M. and Yagi, K. 2001. Investigation of cattle methane production and emission over a 24-hour period using measurements of ^{13}C and D of emitted CH_4 and rumen water. *J. Geophys. Res. 106*, 15405–15413. doi:10.1029/2001JD900177

Borsdorff, T., Brugh, J., Aan de, Pandey, S., Hasekamp, O., Aben, I. and co-authors. 2019. Carbon monoxide air pollution on sub-city scales and along arterial roads detected

by the Tropospheric Monitoring Instrument. *Atmos. Chem. Phys. 19*, 3579–3588. doi:10.5194/acp-19-3579-2019

Bousquet, P., Ciais, P., Miller, J. B., Dlugokencky, E. J., Hauglustaine, D. A. and co-authors. 2006. Contribution of anthropogenic and natural sources to atmospheric methane variability. *Nature 443*, 439–443. doi:10.1038/nature05132

Bréas, O., Guillou, C., Reniero, F. and Wada, E. 2001. The global methane cycle: isotopes and mixing ratios, sources and sinks. *Isotopes Environ. Health Stud. 37*, 257–379. doi:10.1080/10256010108033302

Cain, M., Warwick, N. J., Fisher, R. E., Lowry, D., Lanoisellé, M. and co-authors. 2017. A cautionary tale: a study of a methane enhancement over the North Sea. *J. Geophys. Res. Atmos. 122*, 7630–7645. doi:10.1002/2017JD026626

Chanton, J. P., Rutkowski, C. M., Schwartz, C. C., Ward, D. E. and Boring, L. 2000. Factors influencing the stable carbon isotopic signature of methane from combustion and biomass burning. *J. Geophys. Res. 105*, 1867–1877. doi:10.1029/1999JD900909

Chen, H., Winderlich, J., Gerbig, C., Hoefer, A., Rella, C. W. and co-authors. 2010. High-accuracy continuous airborne measurements of greenhouse gases (CO_2 and $CH_{4)}$ using the cavity ring-down spectroscopy (CRDS) technique. *Atmos. Meas. Tech. 3*, 375–386. doi:10.5194/amt-3-375-2010

Dlugockenky, E. J., Crotwell, A. M., Mund, J. W., Crotwell, M. J. and Thoning, K. W. 2019. Atmospheric methane dry air mole fractions from the NOAA ESRL carbon cycle cooperative global air sampling network, 1983-2018, Version: 2019-07. Online at: https://www.esrl.noaa.gov/gmd/dv/data/index.php?category=Greenhouse

Dlugokencky, E. J., Nisbet, E. G., Fisher, R. and Lowry, D. 2011. Global atmospheric methane: budget, changes and dangers. *Philos. Trans. A Math. Phys. Eng. Sci. 369*, 2058–2072.

EEA (European Environment Agency). 2000. *EMEP/CORINAIR atmospheric emission inventory guidebook - Second edition 1999*. Output from Annual Management Plan. Online at: https://www.eea.europa.eu/publications/EMEPCORINAIR

European Union. 1995. *Eurostat*. European Commission website. Online at: https://ec.europa.eu/eurostat/statistical-atlas/gis/viewer/?

Eyer, S., Tuzson, B., Popa, M. E., van der Veen, C., Röckmann, T. and co-authors. 2016. Real-time analysis of ^{13}C- and D-CH_4 in ambient air with laser spectroscopy: method development and first intercomparison results. *Atmos. Meas. Tech. 9*, 263–280. doi:10.5194/amt-9-263-2016

Fortems-Cheiney, A., Pison, I., Dufour, G., Broquet, G., Berchet, A. and co-authors. 2019. *Variational regional inverse modeling of reactive species emissions with PYVAR-CHIMERE*. Preprint. *Atmos. Sci*. Online at: https://www.geosci-model-dev-discuss.net/gmd-2019-186/

Galand, P. E., Yrjälä, K. and Conrad, R. 2010. Stable carbon isotope fractionation during methanogenesis in three boreal peatland ecosystems. *Biogeosciences 7*, 3893–3900. doi:10.5194/bg-7-3893-2010

Games, L. M. and Hayes, J. M. 1976. On the mechanisms of CO_2 and CH_4 production in natural anaerobic environments. *Environ. Biogeochem. 1*, 51–73.

Happell, J. D., Chanton, J. P. and Showers, W. J. 1995. Methane transfer across the water-air interface in stagnant wooded swamps of Florida: evaluation of mass-transfer coefficients and isotropic fractionation. *Limnol. Oceanogr. 40*, 290–298. doi:10.4319/lo.1995.40.2.0290

Henne, S., Brunner, D., Oney, B., Leuenberger, M., Eugster, W. and co-authors. 2016. Validation of the Swiss methane emission inventory by atmospheric observations and inverse modelling. *Atmos. Chem. Phys. 16*, 3683–3710. doi:10.5194/acp-16-3683-2016

Hitchman, S.P., 1989. Stable isotope ratios in methane containing gasess in the United Kingdom. Technical Report WE/89/30. British Geological Survey.

Hitchman, S. P., 1989. Stable Isotope Ratios in Methane Containing Gasess in the United Kingdom. Technical Report WE/89/30. British Geological Survey.

Hourdin, F., Musat, I., Bony, S., Braconnot, P., Codron, F. and co-authors. 2006. The LMDZ4 general circulation model: climate performance and sensitivity to parametrized physics with emphasis on tropical convection. *Clim. Dyn. 27*, 787–813. doi:10.1007/s00382-006-0158-0

Houweling, S., Krol, M., Bergamaschi, P., Frankenberg, C., Dlugokencky, E. J. and co-authors. 2014. A multi-year methane inversion using SCIAMACHY, accounting for systematic errors using TCCON measurements. *Atmos. Chem. Phys. 14*, 3991–4012. doi:10.5194/acp-14-3991-2014

Hu, H., Landgraf, J., Detmers, R., Borsdorff, T., Brugh, J. and co-authors. 2018. Toward global mapping of methane with TROPOMI: first results and intersatellite comparison to GOSAT. *Geophys. Res. Lett. 45*, 3682–3689. doi:10.1002/2018GL077259

IPCC 2013. *Climate Change 2013: The Physical Science Basis; Working Group I Contribution to the Fifth Assessment Report of the Intergovernmental Panel on Climate Change* (OCLC: 871571414). Cambridge University Press, Cambridge, UK.

Jacob, D. J., Turner, A. J., Maasakkers, J. D., Sheng, J., Sun, K. and co-authors. 2016. Satellite observations of atmospheric methane and their value for quantifying methane emissions. *Atmos. Chem. Phys. 16*, 14371–14396. doi:10.5194/acp-16-14371-2016

Janssens-Maenhout, G., Crippa, M., Guizzardi, D., Muntean, M., Schaaf, E. and co-authors. 2019. EDGAR v4.3.2 global atlas of the three major greenhousegas emissions for the period 1970-2012. *Earth Syst. Sci. Data* 11.3, 959–1002. doi:10.5194/essd-11-959-2019

Keeling, C. D. 1961. The concentration and isotopic abundances of carbon dioxide in rural and marine air. *Geochim. Cosmochim. Acta. 24*, 277–298. doi:10.1016/0016-7037(61)90023-0

Kirschke, S., Bousquet, P., Ciais, P., Saunois, M., Canadell, J. G. and co-authors. 2013. Three decades of global methane sources and sinks. *Nat. Geosci. 6*, 813–823. doi:10.1038/ngeo1955

Klevenhusen, F., Bernasconi, S. M., Kreuzer, M. and Soliva, C. R. 2010. Experimental validation of the Intergovernmental Panel on Climate Change default values for ruminant-derived methane and its carbon-isotope signature. *Anim. Prod. Sci. 50*, 159. doi:10.1071/AN09112

Kuenen, J. J. P., Visschedijk, A. J. H., Jozwicka, M., Gon, H. A. C. and Denier van der, 2014. TNO-MACC_ii emission inventory; a multi-year (2003-2009) consistent high-resolution European emission inventory for air quality modelling. *Atmos. Chem. Phys 14*, 10963–10976. doi:10.5194/acp-14-10963-2014

Levin, I., Bergamaschi, P., Dörr, H. and Trapp, D. 1993. Stable isotopic signature of methane from major sources in Germany. *Chemosphere 26*, 161–177. doi:10.1016/0045-6535(93)90419-6

Levin, I., Glatzel-Mattheier, H., Marik, T., Cuntz, M., Schmidt, M. and co-authors. 1999. Verification of German methane emission inventories and their recent changes based on atmospheric observations. *J. Geophys. Res. 104*, 3447–3456. doi:10.1029/1998JD100064

Lowry, D., Holmes, C. W., Rata, N. D., O'Brien, P. and Nisbet, E. G. 2001. London methane emissions: use of diurnal changes in concentration and d^{13} C to identify urban sources and verify inventories. *J. Geophys. Res. 106*, 7427–7448. doi:10.1029/2000JD900601

Mailler, S., Menut, L., Khvorostyanov, D., Valari, M., Couvidat, F. and co-authors. 2017. CHIMERE-2017: from urban to hemispheric chemistry-transport modeling. *Geosci. Model Dev. 10*, 2397–2423. doi:10.5194/gmd-10-2397-2017

Marécal, V., Peuch, V.-H., Andersson, C., Andersson, S., Arteta, J. and co-authors. 2015. A regional air quality forecasting system over Europe: the MACC-II daily ensemble production. *Geosci. Model Dev.* **8**, 2777–2813. doi:10.5194/gmd-8-2777-2015

Martens, C. S., Kelley, C. A., Chanton, J. P. and Showers, W. J. 1992. Carbon and hydrogen isotopic characterization of methane from wetlands and lakes of the Yukon-Kuskokwim delta, western Alaska. *J. Geophys. Res. 97*, 16689. doi:10.1029/91JD02885

Menut, L., Bessagnet, B., Khvorostyanov, D., Beekmann, M., Blond, N. and co-authors. 2013. CHIMERE 2013: a model for regional atmospheric composition modelling. *Geosci. Model Dev. 6*, 981–1028. doi:10.5194/gmd-6-981-2013

Ministerie van Economische Zaken, TNO. 2018. *Overview of all boreholes.* Online at: https://www.nlog.nl/en/map-boreholes

Monteil, G., Houweling, S., Butz, A., Guerlet, S., Schepers, D. and co-authors. 2013. Comparison of CH_4 inversions based on 15 months of GOSAT and SCIAMACHY observations: INVERSE MODELING OF SATELLITE RETRIEVED *X* CH_4. *J. Geophys. Res. Atmos. 118*, 11,807–11,823. doi:10.1002/2013JD019760

Monteil, G., Houweling, S., Dlugockenky, E. J., Maenhout, G., Vaughn, B. H. and co-authors. 2011. Interpreting methane variations in the past two decades using measurements of CH_4 mixing ratio and isotopic composition. *Atmos. Chem. Phys. 11*, 9141–9153. doi:10.5194/acp-11-9141-2011

Nakagawa, F., Tsunogai, U., Komatsu, D. D., Yamada, K., Yoshida, N. and co-authors. 2005. Automobile exhaust as a source of ^{13} C- and D-enriched atmospheric methane in urban areas. *Org. Geochem. 36*, 727–738. doi:10.1016/j.orggeochem.2005.01.003

Nisbet, E. G., Manning, M. R., Dlugokencky, E. J., Fisher, R. E., Lowry, D. and co-authors. 2019. Very strong atmospheric methane growth in the 4 years 2014–2017: implications for the Paris agreement. *Global Biogeochem. Cycles 33*, 318–342. doi:10.1029/2018GB006009

OSPAR Commission. 2015. *2015 Update of the Inventory of Oil and Gas Offshore Installations in the OSPAR Maritime Area*. OSPAR Commission, Offshore Industry Series. London, UK.

Pandey, S., Houweling, S., Krol, M., Aben, I., Monteil, G. and co-authors. 2017. Enhanced methane emissions from tropical wetlands during the 2011 La Niña. *Sci. Rep. 7*, 45759. doi:10.1038/srep45759

Pandey, S., Houweling, S., Krol, M., Aben, I., Nechita–Banda, N. and co-authors. 2019. Influence of atmospheric transport on estimates of variability in the global methane burden. *Geophys. Res. Lett. 46*, 2302–2311. doi:10.1029/2018GL081092

Pataki, D. E., Ehleringer, J. R., Flanagan, L. B., Yakir, D., Bowling, D. R. and co-authors. 2003. The application and interpretation of Keeling plots in terrestrial carbon cycle research: application of Keeling plots. *Global Biogeochem. Cycles 17*, 1022. doi:10.1029/2001GB001850.

Pisso, I., Sollum, E., Grythe, H., Kristiansen, N., Cassiani, M. and co-authors. 2019. The Lagrangian particle dispersion model FLEXPART version 10.3. *Geosci. Model Dev. Discuss.* 1–67. Retrieved from https://www.geosci-model-dev-discuss.net/gmd-2018-333/

Prinn, R., Weiss, R., Krummel, P., O'Doherty, S. and Muhle, J. 2008. *The ALE/GAGE/AGAGE Network (DB1001)*. Environmental System Science Data Infrastructure for a Virtual Ecosystem; Carbon Dioxide Information Analysis Center (CDIAC), Oak Ridge National Laboratory (ORNL), Oak Ridge, TN.

Rella, C. W., Chen, H., Andrews, A. E., Filges, A., Gerbig, C. and co-authors. 2013. High accuracy measurements of dry mole fractions of carbon dioxide and methane in humid air. *Atmos. Meas. Tech. 6*, 837–860. doi:10.5194/amt-6-837-2013

Riddick, S. N., Mauzerall, D. L., Celia, M., Harris, N. R. P., Allen, G. and co-authors. 2019. Measuring methane emissions from oil and gas platforms in the North Sea. *Atmos. Chem. Phys. Discuss. 19*, 9787–9796. doi:10.5194/acp-2019-90

Rigby, M., Manning, A. J. and Prinn, R. G. 2012. The value of high-frequency high-precision methane isotopologue measurements for source and sink estimation: methane isotopologues in inversions. *J. Geophys. Res. 117,* D12312, 1–14. doi:10.1029/2011JD017384

Ringeval, B., Friedlingstein, P., Koven, C., Ciais, P., de Noblet-Ducoudré, N. and co-authors. 2011. Climate-CH_4 feedback from wetlands and its interaction with the climate-CO_2 feedback. *Biogeosciences 8*, 2137–2157. doi:10.5194/bg-8-2137-2011

Röckmann, T., Eyer, S., Veen, C., van der, Popa, M. E., Tuzson, B. and co-authors. 2016. In situ observations of the

isotopic composition of methane at the Cabauw tall tower site. *Atmos. Chem. Phys. 16*, 10469–10487. doi:10.5194/acp-16-10469-2016

Santoni, G. W., Lee, B. H., Goodrich, J. P., Varner, R. K., Crill, P. M. and co-authors. 2012. Mass fluxes and isofluxes of methane (CH_4) at a New Hampshire fen measured by a continuous wave quantum cascade laser spectrometer: methane isofluxes at a New Hampshire fen. *J. Geophys. Res. 117*, 1–15. Retrieved from http://doi.wiley.com/10.1029/2011JD016960

Saunois, M., Bousquet, P., Poulter, B., Peregon, A., Ciais, P. and co-authors. 2016. The global methane budget 2000–2012. *Earth Syst. Sci. Data 8*, 697–751. doi:10.5194/essd-8-697-2016

Schaefer, H., Fletcher, S. E. M., Veidt, C., Lassey, K. R., Brailsford, G. W. and co-authors. 2016. A 21st-century shift from fossil-fuel to biogenic methane emissions indicated by $^{13}CH\square$. *Science 352*, 80–84. doi:10.1126/science.aad2705

Seibert, P. and Frank, A. 2004. Source-receptor matrix calculation with a Lagrangian particle dispersion model in backward mode. *Atmos. Chem. Phys. 4*, 51–63. doi:10.5194/acp-4-51-2004

Smith, L. K., Lewis, W. M., Jr., Chanton, J. P., Cronin, G. and Hamilton, S. K. 2000. Methane emissions from the Orinoco River floodplain, Venezuela. *Biogeochemistry 51*, 113–140. doi:10.1023/A:1006443429909

Sperlich, P., Uitslag, N. A. M., Richter, J. M., Rothe, M., Geilmann, H. and co-authors. 2016. Development and evaluation of a suite of isotope reference gases for methane in air. *Atmos. Meas. Tech. 9*, 3717–3737. doi:10.5194/amt-9-3717-2016

Stortplaatsen in Nederland. 2019. Online at: https://www.bodemplus.nl/onderwerpen/bodem-ondergrond/verwerking-grond/stortplaatsen/stortplaatsen/

Sugimoto, A. and Fujita, N. 2006. Hydrogen concentration and stable isotopic composition of methane in bubble gas observed in a natural wetland. *Biogeochemistry 81*, 33–44. doi:10.1007/s10533-006-9028-4

Szénási, B. 2019. *Forward modelling simulations of CH_4 and isotopologues* (Deliverable 3.3). Online at: https://h2020-memo2.eu/wp-content/uploads/sites/198/2019/09/Deliverable_D3_3_final_version-SW.pdf

Tarasova, O., Brenninkmeijer, C., Assonov, S., Elansky, N., Rockmann, T. and co-authors. 2006. Atmospheric CH4 along the Trans-Siberian railroad (TROICA) and river Ob: source identification using stable isotope analysis. *Atmos. Environ. 40*, 5617–5628. doi:10.1016/j.atmosenv.2006.04.065

Thanwerdas, J., Saunois, M., Berchet, A., Pison, I., Hauglustaine, D. and co-authors. 2019. Impact of atomic chlorine on the modelling of total methane and its ^{13}C:^{12}C isotopic ratio at global scale. *Atmos. Chem. Phys. Discuss.* In review. doi:10.5194/acp-2019-925

Thielemann, T., Cramer, B. and Schippers, A. 2004. Coalbed methane in the Ruhr Basin, Germany: a renewable energy resource? *Org. Geochem. 35*, 1537–1549. doi:10.1016/S0146-6380(04)00120-2

Townsend-Small, A., Botner, E. C., Jimenez, K. L., Schroeder, J. R., Blake, N. J. and co-authors. 2016. Using stable isotopes of hydrogen to quantify biogenic and thermogenic atmospheric methane sources: a case study from the Colorado Front Range: hydrogen isotopes in the Front Range. *Geophys. Res. Lett. 43*, 11,462–11,471. doi:10.1002/2016GL071438

Turner, A. J., Frankenberg, C. and Kort, E. A. 2019. Interpreting contemporary trends in atmospheric methane. *Proc Natl Acad Sci USA 116*, 2805–2813. doi:10.1073/pnas.1814297116

Tyler, S. C., Bilek, R. S., Sass, R. L. and Fisher, F. M. 1997. Methane oxidation and pathways of production in a Texas paddy field deduced from measurements of flux, d^{13} C, and dD of CH_4. *Global Biogeochem. Cycles 11*, 323–348. doi:10.1029/97GB01624

Tyler, S. C., Blake, D. R. and Rowland, F. S. 1987. $^{13}C/^{12}$ C ratio in methane from the flooded Amazon forest. *J. Geophys. Res. 92*, 1044. doi:10.1029/JD092iD01p01044

Umezawa, T., Brenninkmeijer, C. A. M., Röckmann, T., Veen, C., van der, Tyler, S. C. and co-authors. 2018. Interlaboratory comparison of ^{13} C and D measurements of atmospheric CH_4 for combined use of data sets from different laboratories. *Atmos. Meas. Tech. 11*, 1207–1231. doi:10.5194/amt-11-1207-2018

Uzaki, M., Mizutani, H. and Wada, E. 1991. Carbon isotope composition of CH_4 from rice paddies in Japan. *Biogeochemistry 13*, 159–175.

Vlek, C. 2018. Induced earthquakes from long-term gas extraction in Groningen, the Netherlands: statistical analysis and prognosis for acceptable-risk regulation: induced earthquakes from long-term gas extraction in Groningen. *Risk Anal. 38*, 1455–1473. doi:10.1111/risa.12967

Wageningen University & Research. 2015. *Landelijk Grondgebruik Nederland - LGN7_BRP2015.* Online at: https://www.wur.nl/nl/Onderzoek-Resultaten/Onderzoeksinstituten/Environmental-Research/Faciliteiten-Producten/Kaarten-en-GIS-bestanden/Landelijk-Grondgebruik-Nederland/lgn_viewer.htm

Werner, R. A. and Brand, W. A. 2001. Referencing strategies and techniques in stable isotope ratio analysis. *Rapid Commun. Mass Spectrom. 15*, 501–519. doi:10.1002/rcm.258

Worden, J. R., Bloom, A. A., Pandey, S., Jiang, Z., Worden, H. M. and co-authors. 2017. Reduced biomass burning emissions reconcile conflicting estimates of the post-2006 atmospheric methane budget. *Nat. Commun. 8*, 2227. doi:10.1038/s41467-017-02246-0

World Meteorological Orgnaization (WMO). 2019. *WMO greenhouse gas bulletin (GHG Bulletin) - No. 15: The state of greenhouse gases in the atmosphere based on global observations through 2018*. Tech. Rep. Global Atmospheric Watch. Online at: https://library.wmo.int/doc_num.php?explnum_id=10100

Yacovitch, T. I., Neininger, B., Herndon, S. C., Gon, H. D., Van der, Jonkers, S. and co-authors. 2018. Methane emissions in the Netherlands: the Groningen field. *Elem. Sci. Anth. 6*, 57. doi:10.1525/elementa.308

Zazzeri, G., Lowry, D., Fisher, R., France, J., Lanoisellé, M. and co-authors. 2015. Plume mapping and isotopic

characterisation of anthropogenic methane sources. *Atmos. Environ. 110*, 151–162. doi:10.1016/j.atmosenv.2015.03.029

Zazzeri, G., Lowry, D., Fisher, R. E., France, J. L., Lanoisellé, M. and co-authors. 2016. Carbon isotopic signature of coal-derived methane emissions to the atmosphere: from coalification to alteration. *Atmos. Chem. Phys. 16*, 13669–13680. doi:10.5194/acp-16-13669-2016

Zazzeri, G., Lowry, D., Fisher, R. E., France, J. L., Lanoisellé, M. and co-authors. 2017. Evaluating methane inventories by isotopic analysis in the London region. *Sci. Rep. 7*, 4854. doi:10.1038/s41598-017-04802-6